Short-crested waves in deep water:
a numerical investigation of recent
laboratory experiments

By DAVID R. FUHRMAN AND PER A. MADSEN

Department of Mechanical Engineering, Technical University of Denmark,
DK-2800 Kgs. Lyngby, Denmark

A numerical study of quasi-steady doubly periodic monochromatic short-crested wave patterns in deep water is conducted using a high-order Boussinesq-type model. Simulations using linear wavemaker conditions in the nonlinear model are initially used to approximate conditions from recent laboratory experiments. The computed patterns share many features with those observed in wavetanks, including bending (both frontwards and backwards) of the wave crests, dipping at the crest centrelines, and a pronounced long modulation in the direction of propagation. A new and simple explanation for these features is provided, involving the release of spurious free first harmonics, due to the neglect of steady third-order components in the three-dimensional wave generation. A comparison with the experimentally observed beat length and amplitude matches the theoretical/numerical predictions well. Additionally, direct inclusion of steady third-order components in the wave generation is shown to reduce significantly the modulations (and other unsteady features), further confirming the explanation. This numerical work makes apparent some previously unknown difficulties associated with the physical generation of even the simplest three-dimensional waves, adding significant insight into the interpretation of recent experimental observations.

1. Introduction

The study of doubly periodic short-crested water waves, which are perhaps the simplest genuinely three-dimensional waveforms, is of fundamental importance to the understanding of the multi-directional irregular sea surface. Short-crested wave patterns are likewise of considerable practical interest, as they commonly arise, for example, from the oblique interaction of two travelling plane waves, from the reflection of waves at non-normal incidence off vertical sea walls, as well as from diffraction about both ends of a finite length structure. They are therefore currently receiving increased experimental, analytical and numerical attention, as extensions beyond the classical two-dimensional description for water waves become more and more common.

At the limit of small amplitudes, progressive monochromatic short-crested wave patterns can be produced through the superposition of two linear oblique progressive waves (with identical amplitude and frequency). However, when nonlinearities are important, the nature of such patterns is widely known to depend on the water depth. In shallow water, waves colliding at oblique incidence are known to produce spectacular hexagonal shapes, as shown experimentally by Hammack, Scheffner &

Segur (1989), and numerically by, e.g. Chen & Liu (1995), Nicholls (1998, 2001) and Craig & Nicholls (2002). Such hexagonal patterns are also commonly observed in coastal regions (see e.g. the photographs of Hammack *et al.* 1995).

Alternatively, in deep water such interactions are known to produce equally spectacular so-called rectangular short-crested waveforms with straightened crestlines in the transverse direction and zero nodal lines, as shown analytically by, e.g. Roberts (1983) and Bryant (1985) and numerically by, e.g. Craig & Nicholls (2002). Short-crested wave patterns in deep water have been studied experimentally by, e.g. Kimmoun, Branger & Kharif (1999*a*), who created travelling patterns of nearly permanent form via the sea-wall reflection of incident plane waves, as well as by Hammack, Henderson & Segur (2005) (see also Hammack & Henderson 2003), who generated such patterns directly through a precisely controlled wavemaker system, comprised of multiple side-by-side paddles.

A number of steady short-crested gravity-wave solutions have been presented, e.g. by Hsu, Tsuchiya & Silvester (1979) (see also Fenton 1985), Ioualalen (1993) and Roberts & Peregrine (1983), in addition to those references cited previously. However, the laboratory experiments of Hammack *et al.* (2005), which use linearized wavemaker conditions, are reported to exhibit a number of rather pronounced unsteady features. These include modulations along the direction of propagation, bending of crestlines (both frontwards and backwards), as well as the formation of dips at the centreline of the wave crests. Hammack *et al.* (2005) propose that the observed unsteadiness is largely due to Benjamin & Feir (1967) type instabilities. Our desire to reproduce numerically the spectacular patterns observed in these experiments has been the primary inspiration for the present work, with the hope of providing further insight into the root cause of these particular features. Attempts to reproduce the experimental conditions numerically, to be described in the following, do indeed lead to similar features. By systematically assessing the consequences of using first-order (linear) wavemaker conditions, it will be shown that these unsteady features can in fact be attributed to a non-intuitive, and previously unrecognized, release of spurious free first harmonics due to neglected steady third-order contributions (in terms of Stokes-type expansions) in the three-dimensional wave generation.

The remainder of this paper is organized as follows. The fully nonlinear numerical Boussinesq-type model used throughout this work is described in §2. Nonlinear simulations of short-crested waves in deep water using linearized wavemaker conditions, similar to those used in the experiments, are presented in §3, with the resulting observed phenomena explained in §4. Validation of the physical explanation with additional simulations covering a range of incident angles is provided in §5, and a quantitative comparison with the physical experiments is provided in §6. Additional simulations using third-order incident waves are considered in §7, which greatly reduce the previously noted modulations (and other unsteady features), providing additional confidence in the explanation. Discussion and conclusions are finally provided, respectively, in §§8 and 9.

2. The numerical model

The numerical model used in the present work is based on the recently derived fully nonlinear, highly dispersive Boussinesq-type formulation of Madsen, Bingham & Liu (2002) and Madsen, Bingham & Schäffer (2003). As the method has now been discussed numerous times in the literature, the equations will merely be written here for completeness. This method uses exact representations of the kinematic and dynamic

free-surface conditions expressed in terms of surface quantities as

$$\frac{\partial \eta}{\partial t} = \tilde{w}(1 + \nabla\eta \cdot \nabla\eta) - \tilde{\boldsymbol{U}} \cdot \nabla\eta, \tag{2.1}$$

$$\frac{\partial \tilde{\boldsymbol{U}}}{\partial t} = -g\nabla\eta - \nabla\left(\frac{\tilde{\boldsymbol{U}} \cdot \tilde{\boldsymbol{U}}}{2} - \frac{\tilde{w}^2}{2}(1 + \nabla\eta \cdot \nabla\eta)\right), \tag{2.2}$$

where $\tilde{\boldsymbol{U}} = (\tilde{U}, \tilde{V}) = \tilde{\boldsymbol{u}} + \tilde{w}\nabla\eta$. Here $\tilde{\boldsymbol{u}} = (\tilde{u}, \tilde{v})$ and $\tilde{w}$ are the horizontal and vertical velocities directly on the free surface $z = \eta$, $g = 9.81\,\mathrm{m\,s^{-2}}$ is the acceleration due to gravity, $\nabla = (\partial/\partial x, \partial/\partial y)$ is the horizontal gradient operator, and t is time. Through a Padé-enhanced truncated series solution of the Laplace equation, the vertical distribution of fluid velocity is approximated by

$$\boldsymbol{u}(x, y, z, t) = (1 - \alpha_2\nabla^2 + \alpha_4\nabla^4)\hat{\boldsymbol{u}}^*(x, y, t) + ((z - \hat{z})\nabla - \beta_3\nabla^3 + \beta_5\nabla^5)\hat{w}^*(x, y, t), \tag{2.3}$$

$$w(x, y, z, t) = (1 - \alpha_2\nabla^2 + \alpha_4\nabla^4)\hat{w}^*(x, y, t) - ((z - \hat{z})\nabla - \beta_3\nabla^3 + \beta_5\nabla^5)\hat{\boldsymbol{u}}^*(x, y, t), \tag{2.4}$$

where

$$\left.\begin{array}{ll} \alpha_2 = \dfrac{(z - \hat{z})^2}{2} - \dfrac{\hat{z}^2}{18}, & \alpha_4 = \dfrac{(z - \hat{z})^4}{24} - \dfrac{\hat{z}^2(z - \hat{z})^2}{36} + \dfrac{\hat{z}^4}{504}, \\[3mm] \beta_3 = \dfrac{(z - \hat{z})^3}{6} - \dfrac{\hat{z}^2(z - \hat{z})}{18}, & \beta_5 = \dfrac{(z - \hat{z})^5}{120} - \dfrac{\hat{z}^2(z - \hat{z})^3}{108} + \dfrac{\hat{z}^4(z - \hat{z})}{504}. \end{array}\right\} \tag{2.5}$$

Optimal velocity distributions are obtained with the expansion point near $\hat{z} = -h/2$, and we adopt this value throughout. Considering (2.3) and (2.4) at the sea bottom $z = -h$, the kinematic bottom condition (neglecting bottom slope) becomes

$$\left(1 - \tfrac{4}{9}\gamma^2\nabla^2 + \tfrac{1}{63}\gamma^4\nabla^4\right)\hat{w}^* + \left(\gamma\nabla - \tfrac{1}{9}\gamma^3\nabla^3 + \tfrac{1}{945}\gamma^5\nabla^5\right)\hat{\boldsymbol{u}}^* = 0, \tag{2.6}$$

where $\gamma = (h + \hat{z}) = h/2$. It is straightforward to include variable depth terms; however, as the present work is restricted to flat bottoms, they are not presented here. Analysis of this system has shown that it provides excellent linear and nonlinear dispersive properties and surface quantities to (wavenumber times depth) $kh \approx 25$, and accurate velocity kinematics to $kh \approx 12$, largely eliminating any shallow-water limitations conventionally associated with Boussinesq-type methods. Thus, within a large range of kh, the system may be regarded as a highly accurate approximation to the exact Laplace problem for nonlinear water waves.

The system of PDEs is solved numerically using the scheme originally presented by Fuhrman & Bingham (2004), which combines high-order 37-point finite-difference spatial discretizations with a fourth-order four-stage explicit Runge–Kutta time-stepping scheme. Simulations presented here use the matrix free Fourier space preconditioner and irrotational operators, as discussed therein. Closed transverse boundaries are created by imposing appropriate symmetries about the numerical sidewalls. The numerical stability of the model has been analysed by Fuhrman *et al.* (2004*a*), and the basic finite-difference model has been extended to incorporate rapidly varying bathymetries by Madsen, Fuhrman & Wang (2006), as well as semi-irregular computational domains by Fuhrman, Bingham & Madsen (2005). Additional applications of the model have been presented by Fuhrman, Madsen & Bingham (2004*b*), who studied the highly nonlinear phenomenon of crescent wave patterns, due to the three-dimensional (class II) instability of steep plane waves.

3. Simulations using first-order incident conditions

3.1. *Model set-up*

The basic model set-up used throughout this work consists of an analytic wavemaker region at the left-hand boundary, relaxed over 65 grid points (with $x = 0$ taken as the end of this zone). An additional 65–100 grid-point sponge layer is similarly placed at the right-hand boundary to absorb the outgoing wavefield. In all simulations, a tenth- (polynomial) order 109-point (octagon shaped) Savitzky & Golay (1964) type smoothing filter is applied incrementally to remove high-wavenumber disturbances, which can arise owing to the discretization of the nonlinear terms. A Fourier analysis of this filter (see the Appendix of Fuhrman, Madsen & Bingham 2006) has shown that its dissipative effects are primarily restricted to very high-wavenumber modes (resolved with four or fewer grid points per wavelength). The frequency of application depends on the simulation and will be made apparent.

Throughout this section, short-crested waves are generated in the numerical model by imposing

$$\eta(x, y, t) = a \cos(\omega t - k_x x) \cos(k_y y), \tag{3.1}$$

$$\tilde{U}(x, y, t) = \frac{a\omega k_x}{k} \frac{\cosh kh}{\sinh kh} \cos(\omega t - k_x x) \cos(k_y y), \tag{3.2}$$

$$\tilde{V}(x, y, t) = \frac{a\omega k_y}{k} \frac{\cosh kh}{\sinh kh} \sin(\omega t - k_x x) \sin(k_y y), \tag{3.3}$$

as initial conditions across the entire domain (removing any difficulties from an abrupt incident wavefront), which are then repeated indefinitely in the wavemaker region. These conditions satisfy the linearized water-wave problem (i.e. they correspond to a first-order Stokes-type expansion), and are exact progressive solutions at the limit of small amplitudes. This has been confirmed directly in the numerical model by switching off the nonlinear terms, which indeed results in progressive doubly periodic short-crested waves of permanent form. We are well aware that these incident conditions are not progressive solutions to the fully nonlinear water-wave problem. Their use is warranted in the present context, however, as they correspond closely to the physical (linear) wavemaker conditions used by Hammack *et al.* (2005) in their wavetank experiments C1–C14, where the incident angle and nonlinearity were systematically varied. Hence, the simulations are carried out with the hope of adding insight to some of their observations. Simulations using higher-order wavemaker conditions will be considered in § 7.

Throughout this work, short-crested wave simulations will be characterized by their wave steepness ak, which serves as a measure of nonlinearity, as well as the angle

$$\theta = \tan^{-1}\left(\frac{k_x}{k_y}\right), \tag{3.4}$$

which governs the directionality, with $k_x = k \sin\theta$ and $k_y = k \cos\theta$. Note that under this definition, $\theta = 0°$ corresponds to the standing wave limit, while $\theta = 90°$ corresponds to the plane wave limit. All simulations in the present work are normalized using the wavenumber modulus $k = \sqrt{k_x^2 + k_y^2} = 1\,\text{m}^{-1}$, with dimensionless depth $kh = 2\pi$, i.e. deep water. In the present section, the angular frequency is computed from the linear dispersion relation $\omega = \sqrt{gk \tanh(kh)} = 3.13\,\text{s}^{-1}$, which with $kh = 2\pi$ is essentially equivalent to the deep-water dispersion relation $\omega = \sqrt{gk}$. While the (normalized)

dimensional parameters used here differ from those used in the physical experiments, they will match closely in a dimensionless sense (in terms of both the wave steepness and incident angle). This is justified by basic similitude.

Throughout this work, the spatial discretizations $\Delta x = L_x/32$ and $\Delta y = L_y/32$ are used, where $L_x = 2\pi/k_x$ and $L_y = 2\pi/k_y$, combined with the temporal discretization $\Delta t = \pi/(32\sqrt{gk}) = 0.0313\,\mathrm{s}$, corresponding to 64 time steps per linear period. The model domain consists of a 1025×17 computational grid, and simulations are run for 8000 time steps (i.e. 125 periods), which is sufficient to reach equilibrium throughout the domain.

3.2. *Numerical results*

We begin our simulations by studying the effects of variable wave steepness. Specifically, we will attempt to reproduce numerically (in a non-dimensional sense) cases C9, C12 and C14 from the experiments of Hammack *et al.* (2005), having incident steepness $ak = 0.15$, 0.30 and 0.40, respectively, with a constant incident angle $\theta = 80.79°$. These cases are chosen to represent weakly, moderately and highly nonlinear cases, respectively. In these simulations, the smoothing filter is applied after every 64, 2 and 1 time steps, respectively. As an indication of the computational efficiency, the simulation of case C12 with $ak = 0.30$ requires approximately 6.2 h on a single 3.2 GHz Pentium 4 processor.

Computed free surfaces near the end of the simulations from these three cases are shown in figure 1, covering the first $15L_x$ after the wavemaker region. Note that a full transverse wavelength is produced by simply reflecting the solutions across the numerical sidewall a single time. Case C9 (figure 1*a*) which corresponds to the lowest nonlinearity considered ($ak = 0.15$), expectedly results (at least visually) in progressive doubly periodic short-crested waves of nearly constant form. In contrast, the computed free surface for the steeper cases C12 (figure 1*b*) and C14 (figure 1*c*), clearly demonstrate an unsteady phenomenon. This is most pronounced in the steepest case C14 (with $ak = 0.40$) (figure 1*c*) a top view of which is also shown in figure 2.

Upon closer examination, these simulations can be shown to share many common features with the physical experiments of Hammack *et al.* (2005), on which they are based. Specific examples will be discussed in the following. First, from figure 1(*c*) the wave crests can be seen to, at times, become flattened, while at other times developing either peaks or dips at their centreline, depending on their location. These features are given in table 6 of Hammack *et al.* (2005), and can be clearly seen, for example, in their figures 9 and 14. Additionally, from the top view shown in figure 2, it is clear that the crestlines, at times, become curved either frontwards or backwards, depending on the location within the domain. This curving of the crestlines was also observed in the experiments of Hammack *et al.* (2005), and can clearly be seen from their experimental overhead pictures, especially in the most nonlinear experiments depicted in their figures 9, 14 and 15. These various features can also be clearly seen in the contour plots from the present simulations shown in figure 3, particularly in figures 3(*b*) and 3(*c*).

Perhaps the most pronounced unsteady feature from these simulations, as well as from the experiments, is a curious modulation in the direction of propagation, which seems to drive the other previously mentioned features. This particular phenomenon is more clearly demonstrated in figure 4, which shows the computed free-surface envelope for nearly the entire computational domain along $y = 0$ for each of the three cases considered. Here it is evident that, in fact, none of the three simulations
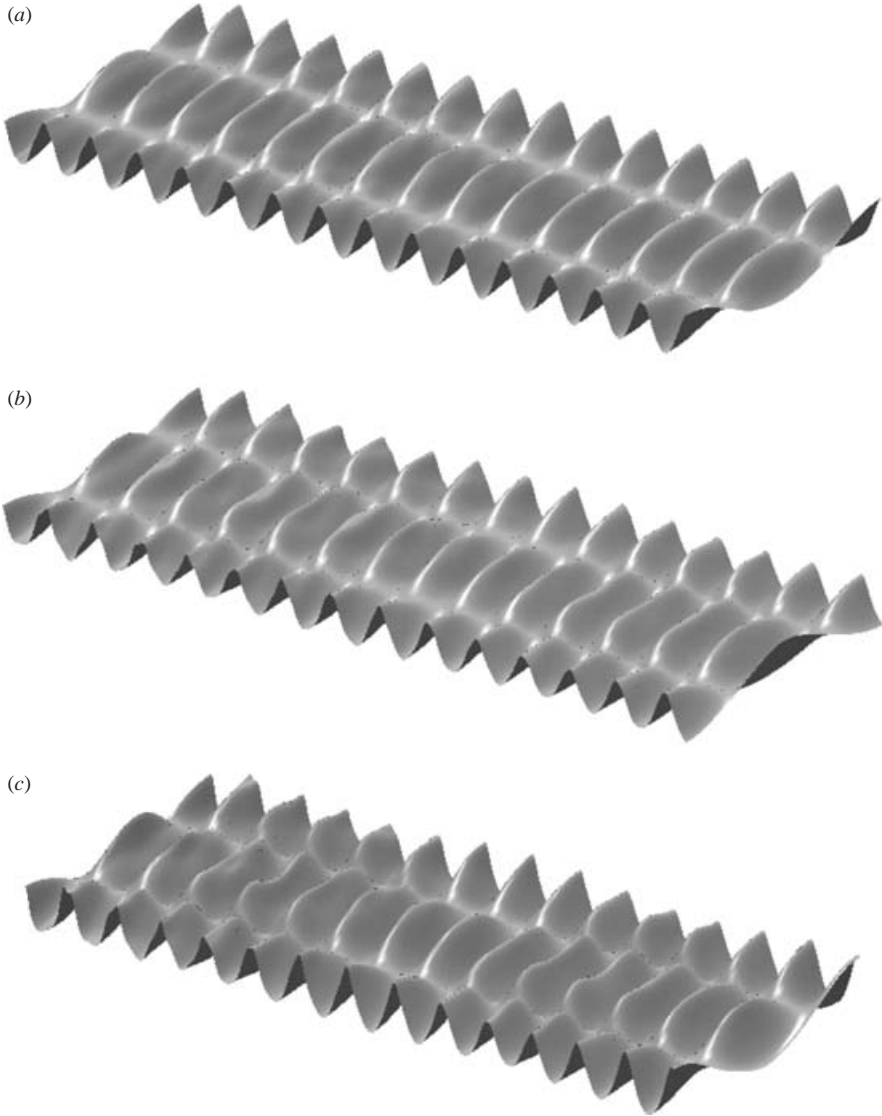
(*a*)

(*b*)

(*c*)

FIGURE 1. Computed free surface for case (*a*) C9 with $ak = 0.15$, (*b*) C12 with $ak = 0.30$, and (*c*) C14 with $ak = 0.40$, all at $t \approx 123.8T$. The vertical scale is exaggerated (*a*) 20 and (*b, c*) 10 times.

result in a steady pattern. Rather, there is a clear modulation of roughly $7L_x$–$9L_x$, even in the weakly nonlinear case C9. The amplitude of the modulation becomes noticeably more pronounced as the wave steepness is increased (consistent with the physical experiments), with the length of the modulation likewise becoming slightly decreased. These computed envelopes bear a strong resemblance to those from, for example, figure 11(*a*) of Hammack *et al.* (2005) (especially their bottom two sub-plots), which show a measured time series from a traverse of the experimental centreline. A quantitative comparison will be made in §6.

   Thus, we conclude that the computed short-crested surface patterns, in many distinct ways, are consistent with those observed in the physical experiments of
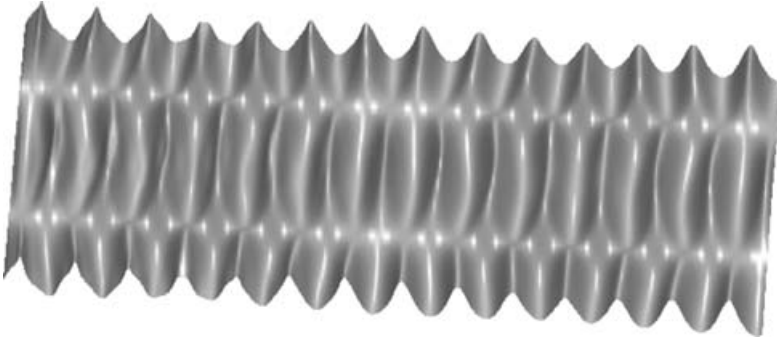
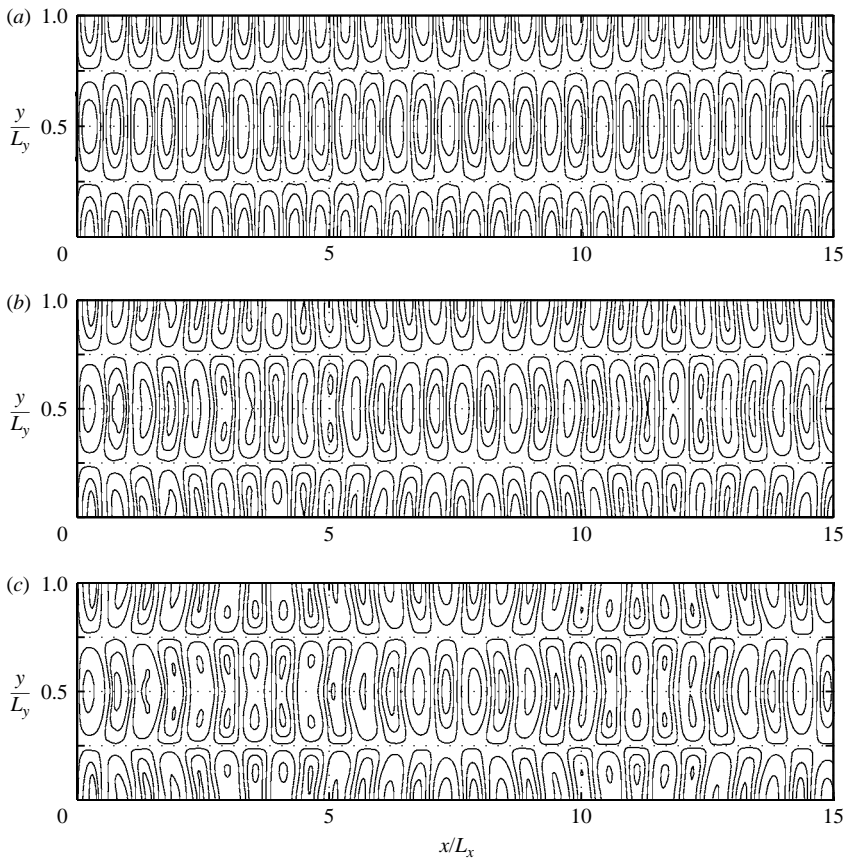FIGURE 2. Computed top view of the free surface for case C14 (with $ak = 0.40$) at $t = 124.2T$.

FIGURE 3. Computed contour plots of the free surface for case (*a*) C9 with $ak = 0.15$, (*b*) C12 with $ak = 0.30$, and (*c*) C14 with $ak = 0.40$, all at $t = 124.2T$.

Hammack *et al.* (2005). This is hardly surprising, given that we have intentionally tried to match their experimental set-up. Establishing this qualitative similarity is a necessary and important first step, however, as we will attempt to explain many of the observed experimental features directly from our numerical simulations in the following section.
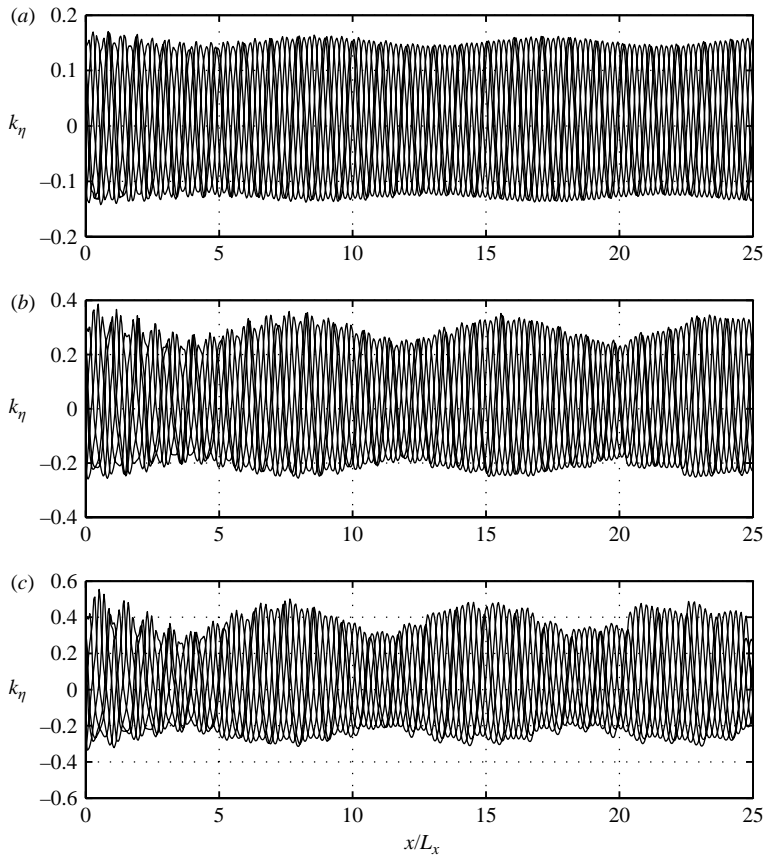
FIGURE 4. Computed surface elevation envelopes along $y = 0$ for case (a) C9 with $ak = 0.15$, (b) C12 with $ak = 0.30$, and (c) C14 with $ak = 0.40$.

4. Physical explanation

Having established that our numerical simulations are qualitatively similar to the physical experiments of Hammack *et al.* (2005), we will now explain their dominant features using simple well-established analysis concepts. More specifically, we will systematically assess the consequences of the first-order short-crested wave generation indicated by (3.1). While the consequences of using low-order generation methods for two-dimensional (plane) waves are well understood, the related effects associated with the generation of genuinely three-dimensional waves have not, to our knowledge, been previously considered.

To gain some insight into the physical cause of the previously noted modulations, figure 5 shows the computed first and second harmonic amplitudes along $y = 0$ in the direction of propagation for the three cases considered. These are computed through a linear-least-squares regression from time series at each grid point. From this figure, there is a rapid (short) beat of the second harmonic amplitude, as well as a slow (long) beat of the first harmonic amplitude. The first harmonic beat is very pronounced, and it is clearly responsible for the large envelope modulations depicted in figure 4.

The rapid beating of the second harmonic is, in fact, a well-known artefact of using linear boundary conditions for nonlinear problems. Because of the omission of bound second harmonic components at the wavemaker boundary, spurious free
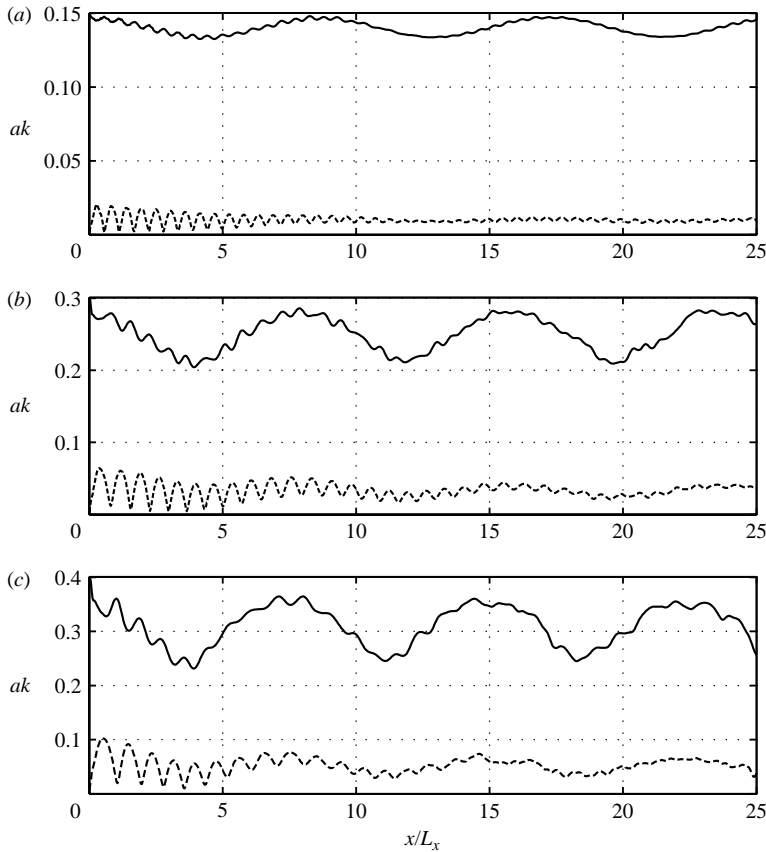
FIGURE 5. Computed first- (full line) and second-harmonic (dashed line) amplitudes along $y = 0$ for case (*a*) C9 with $ak = 0.15$, (*b*) C12 with $ak = 0.30$, and (*c*) C14 with $ak = 0.40$.

second harmonics will be released. The combination of propagating free and bound second harmonics with different wavenumbers will then create a systematic beat in the amplitude at this frequency. This phenomenon is well known from flume tests, and has been studied experimentally by, e.g. Boczar-Karakiewicz (1972), Buhr-Hansen & Svendsen (1974) and Chapalain, Cointe & Temperville (1992); theoretically by, e.g. Mei & Ünlüata (1972), Bryant (1973) and Mei (1983); and numerically by, e.g. Madsen & Sørensen (1993). Within the context of three-dimensional short-crested waves, the phenomenon is slightly more complicated, and will therefore be discussed in what follows.

To assess the release of spurious free waves occurring at a given order, we must first establish the form of the corresponding bound components in the travelling solution. From Hsu *et al.* (1979), their equation (41) (transformed into dimensional variables), the steady second-order surface elevation is

$$\eta^{(2)}_{bound} = a^2 k [b_1 \cos(2k_y y) \cos(2\omega t - 2k_x x) + b_2 \cos(2\omega t - 2k_x x) + b_3 \cos(2k_y y)]. \quad (4.1)$$

The expressions for the various dimensionless b coefficients can be obtained from Hsu *et al.* (1979), and for brevity will not be re-written here. As discussed, e.g. by Madsen & Fuhrman (2006), the form (but not the respective amplitudes) of the bound second-order solution can, in fact, be obtained by simply taking the square of the

incident wavefield (3.1); however, the actual expressions from Hsu *et al.* (1979) will be used here for completeness.

From (4.1), the first two terms correspond to bound second harmonics. The first has the form of a short-crested wave, having the same directionality as the incident wave, while the second is a plane wave travelling in the pure x-direction. The last term represents a set-up, which is constant in x as well as in time. If the first two (time variant) terms are absent in the prescribed incident wave (as is the case here, as well as in the physical experiments), the model will respond by releasing spurious waves, which will propagate as free wave components. These will have equal amplitude, but opposite phase compared to the bound waves at the wavemaker boundary, i.e. they will be oriented so that they cancel the missing bound components at $x = 0$. The spurious free waves will therefore match the frequency and transversal wavenumbers of the corresponding bound waves, while their wavenumbers in the x-direction will adjust to satisfy the linear dispersion relation (assuming weak nonlinearity). The second-order spurious wavefield will thus be of the form

$$\eta_{free}^{(2)} = -a^2 k [b_1 \cos(2k_y y) \cos(2\omega t - k_{21} x) + b_2 \cos(2\omega t - k_{22} x)], \qquad (4.2)$$

consisting of a free short-crested wave, as well as a free plane wave, both with frequency 2ω. These two spurious waves will approximately satisfy the linear deep-water dispersion relations

$$\sqrt{k_{21}^2 + (2k_y)^2} = \frac{(2\omega)^2}{g} = 4k, \qquad k_{22} = \frac{(2\omega)^2}{g} = 4k, \qquad (4.3)$$

where the former equation leads to

$$k_{21} = 2k\sqrt{4 - \cos^2\theta}. \qquad (4.4)$$

From simple superposition arguments, the presence of these two free waves yields three potential second harmonic beat lengths. The first two are due to differences in the x-wavenumber components of the bound and free waves, and can be approximated by

$$L_{B21} = \frac{2\pi}{k_{21} - 2k_x}, \qquad L_{B22} = \frac{2\pi}{k_{22} - 2k_x}. \qquad (4.5)$$

The third beat length is potentially due to differences between the two free wave components, and can be approximated by

$$L_{B23} = \frac{2\pi}{k_{22} - k_{21}}. \qquad (4.6)$$

It is convenient to relate the beat lengths directly to the incident wavelength L_x. In such a dimensionless form, expressed in terms of the angle θ, (4.5) and (4.6), respectively, become

$$\frac{L_{B21}}{L_x} = \frac{\sin\theta}{2\sqrt{4 - \cos^2\theta} - 2\sin\theta}, \qquad \frac{L_{B22}}{L_x} = \frac{\sin\theta}{4 - 2\sin\theta}, \qquad (4.7)$$

$$\frac{L_{B23}}{L_x} = \frac{\sin\theta}{4 - 2\sqrt{4 - \cos^2\theta}}. \qquad (4.8)$$

Note that as θ approaches $90°$, $L_{B21} \approx L_{B22}$ ($\approx L_x/2$), and consequently L_{B23} becomes very long. For the case considered in §3 with $\theta = 80.79°$, the beat lengths from (4.7) and (4.8) are: $L_{B21} = 0.490 L_x$, $L_{B22} = 0.487 L_x$ and $L_{B23} = 76.9 L_x$. The first two are almost identical, and match reasonably the observed beat length in figure 5(a),
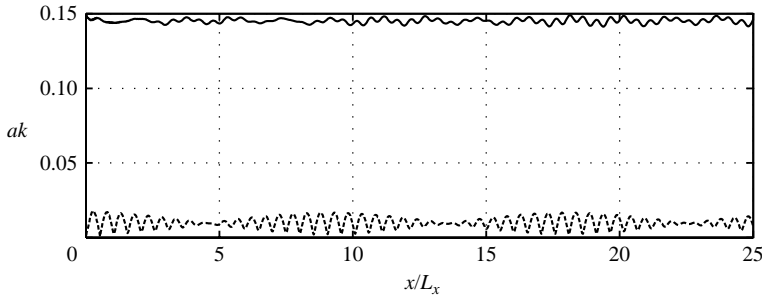
FIGURE 6. Computed first- (full line) and second-harmonic (dashed line) amplitudes along $y = 0$ from a short-crested wave simulation with $ak = 0.15$ and $\theta = 72.5°$.

corresponding to the case with the lowest nonlinearity (note that at larger steepness these tend to increase, as seen in figure 5b, c). L_{B23} is too long to be captured within the computational domain, though beating of the second harmonic is clearly diminishing along the channel.

To illustrate more clearly the second harmonic beat length L_{B23}, we consider an additional simulation using $ak = 0.15$ and $\theta = 72.5°$, with the harmonic amplitudes presented in figure 6. For this case, the predicted beat lengths from (4.7) and (4.8) are: $L_{B21} = 0.466L_x$, $L_{B22} = 0.456L_x$ and $L_{B23} = 21.0L_x$. The first two are again similar, and match reasonably the rapid second harmonic beat length seen in figure 6. As before, this case initially leads to a gradual disappearance of the second harmonic beat, which is now followed by a reappearance. The beat length L_{B23} in fact spans two such cycles, as the second harmonic will have maximum modulation at both the trough and peak of the corresponding group length. The computed beat length in this case $L_{B23} \approx 18L_x$ is, in fact, slightly less than predicted, probably due to finite-amplitude effects. This confirms the presence of this additional second harmonic beat length.

The beat of the second harmonic is a relatively minor feature of these simulations, however, with the much more prominent long modulations seen in figure 4 clearly driven by the (as yet unexplained) beat of the first harmonic. To explain this first harmonic modulation, we must continue our evaluation to third order. As discussed, e.g. by Madsen & Fuhrman (2006), the form (but not the respective amplitudes) of the steady third-order surface elevation can be established simply by evaluating the square of the sum of first- and second-order solutions, which is equivalent to a cubic power of the first-order solution (3.1). For completeness, however, we will again use the expressions from the steady solution of Hsu *et al.* (1979), with the b (dimensionless amplitude) coefficients as given therein. From their equation (58) (expressed in a dimensional form), the steady third-order surface elevation reads

$$\eta_{bound}^{(3)} = \frac{a^3 k^2}{2}[b_{11}\cos(k_y y)\cos(\omega t - k_x x) + b_{13}\cos(3k_y y)\cos(\omega t - k_x x)$$
$$+ b_{31}\cos(k_y y)\cos(3\omega t - 3k_x x) + b_{33}\cos(3k_y y)\cos(3\omega t - 3k_x x)]. \quad (4.9)$$

The first (b_{11}) term in (4.9) has the same form as the prescribed incident wave (3.1), representing a third-order correction to the first-order amplitude. This term was added by Hsu *et al.* (1979) in order to eliminate third-order secular terms, which is an arbitrary choice and could alternatively be added to the velocity potential (see Madsen & Fuhrman 2006). Hence we shall neglect this term in the following

discussion. The last three terms in (4.9), having non-dimensional amplitudes b_{13}, b_{31} and b_{33}, represent bound waves. Similarly to before, neglecting these three terms in the wave generation (as done here, as well as in the experiments) will lead to the release of three corresponding spurious free waves. These will again match the frequencies and y-wavenumbers of the corresponding bound waves, but with adjusted x-wavenumber components. The third-order spurious wavefield will then be of the form

$$\eta_{free}^{(3)} = -\frac{a^3 k^2}{2} [b_{13} \cos(3k_y y) \cos(\omega t - k_{13} x)$$
$$+ b_{31} \cos(k_y y) \cos(3\omega t - k_{31} x) + b_{33} \cos(3k_y y) \cos(3\omega t - k_{33} x)]. \quad (4.10)$$

The presence of the last two terms from (4.10) will result in modulations of the third harmonic amplitude. These have indeed been detected from the model, though we will not focus on them here. The spurious free wave stemming from the first term in (4.10) is more interesting in the present context, as it will create modulations in the first harmonic amplitude, potentially explaining the behaviour seen in figure 5. As a first estimate, we may again assume that the free waves from (4.10) satisfy the linear deep-water dispersion relation. For the spurious free first harmonic this leads to

$$\sqrt{k_{13}^2 + (3k_y)^2} = \frac{\omega^2}{g} = k, \quad (4.11)$$

where solving for k_{13} finally gives

$$k_{13} = \sqrt{k^2 - (3k_y)^2} = k\sqrt{1 - 9\cos^2\theta}. \quad (4.12)$$

The x-variation of the first harmonic amplitude is therefore caused by the difference in the x-wavenumber components of the incident and spurious free waves, and the resulting beat length can be approximated by

$$L_B = \frac{2\pi}{k_x - k_{13}}, \quad (4.13)$$

or in dimensionless form

$$\frac{L_B}{L_x} = \frac{\sin\theta}{\sin\theta - \sqrt{1 - 9\cos^2\theta}}. \quad (4.14)$$

For the cases with $\theta = 80.79°$ this gives $L_B = 8.98 L_x$, closely matching the observed first harmonic beat length observed, e.g. in figure 5(*a*). This confirms the present explanation, at least for the simulations considered.

   The explanation of this first-harmonic beat is new. It is due entirely to the three-dimensionality of the problem, and will disappear at the plane wave limit (where it becomes infinitely long), which probably explains why it has not been previously made apparent. Note also from (4.12) that k_{13} can become complex when the quantity within the square root is negative. Therefore, these spurious free first harmonics can only exist as progressive wave modes when the threshold

$$\cos\theta < \tfrac{1}{3}, \quad (4.15)$$

is satisfied. This corresponds to $\theta > 70.53°$, i.e. the phenomenon is restricted to relatively large incident angles. At this threshold $L_B = L_x$, i.e. the modulation length matches the incident wavelength. It is worth mentioning that all of the experiments from Hammack *et al.* (2005) satisfy the criterion from (4.15), and all were reported to exhibit modulations along the direction of propagation. In contrast, the earlier
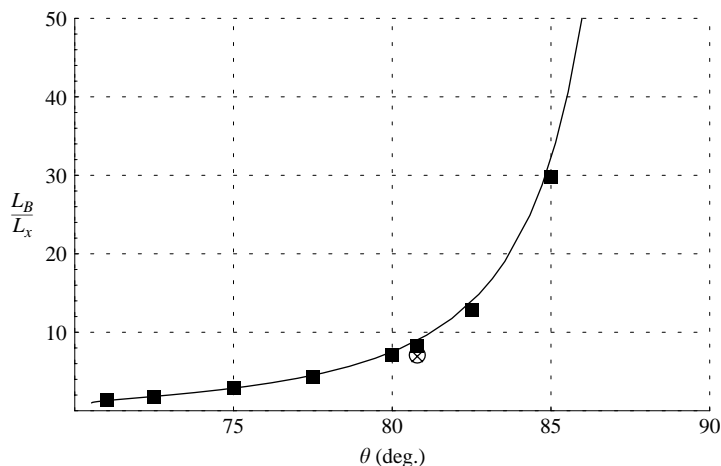
FIGURE 7. Comparison of the theoretical (line, from (4.14)) and computed (squares) beat length of the first harmonic amplitude. The computed points are from simulations with steepness $ak = 0.15$, except for the case with $\theta = 85°$ where $ak = 0.10$. The additional $\circ$ marks the computed beat length for case C14 (with $ak = 0.40$) from figure 5(c), while $\times$ marks the corresponding experimental value estimated from figure 11(a) (bottom sub-figure) of Hammack *et al.* (2005).

short-crested wavetank experiments of Kimmoun *et al.* (1999a) were restricted to $\theta \leqslant 45°$ and showed no evidence of such a beat. Thus, observations from both sets of physical experiments are consistent with the present explanation.

The other features mentioned earlier, i.e. bending wave crests, and peaks or dips at the crest centrelines (see again figures 1, 2 and 3), are clearly related to the first harmonic modulation, as their respective evolutions all follow the same beat length. The bending crests, either frontwards or backwards, can be explained simply through the phase of the spurious first harmonic relative to the primary short-crested wave. If the peak of the spurious free wave at a given location is slightly in front of or behind a primary wave crest, it will, respectively, appear to bend it frontwards or backwards. Peaks/dips along the centreline will similarly occur at locations where a primary wave crest is in phase with a peak/trough of a spurious free first harmonic (which has transversal wavenumber $3k_y$), provided that it is of sufficient amplitude. Thus all of these unsteady features are in fact closely related, and can be explained in a unified fashion from this phenomenon.

5. Validation against additional simulations

Further confirmation of the first harmonic beat length explained in the previous section is provided in figure 7, which demonstrates a comparison of the predicted values of L_B/L_x from (4.14) with results from additional numerical simulations (having low steepness, shown as squares), where θ is varied. The case with $\theta = 80.79°$ corresponds to case C9, while that with $\theta = 72.5°$ is depicted in figure 6. As can be seen, in each of the simulations, the match in the first harmonic beat length compares extremely well with the theoretical predictions. Note also that a simulation with $\theta = 70°$ shows no sign of the spurious first harmonic, whereas with $\theta = 71°$ the modulation is as predicted (see figure 7), directly confirming the threshold from (4.15).
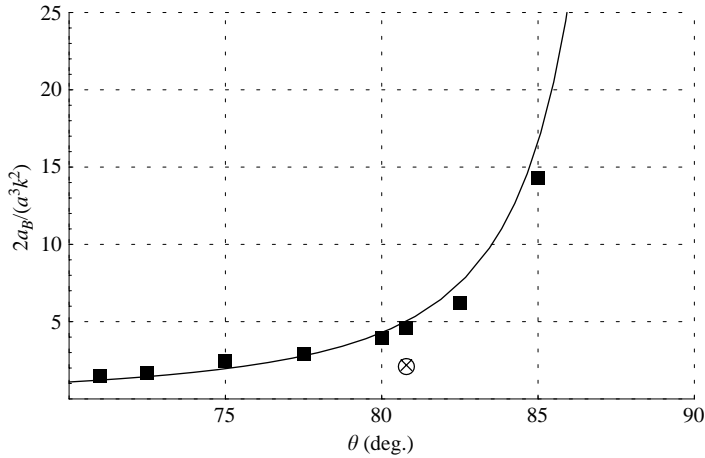
FIGURE 8. Comparison of the computed (dimensionless and normalized) spurious first harmonic amplitude from simulations (squares, from the same series as in figure 7) with the absolute value of the b_{13} coefficient (line) from (5.1). ○, computed; ×, experimental values from case C14, with $ak = 0.40$.

As discussed previously, the amplitudes of the spuriously generated free waves may be estimated directly from those of the corresponding neglected terms in the steady third-order solution. For the case of the spurious free first harmonic, as already indicated in (4.10), this corresponds to the dimensionless coefficient b_{13}. From equation (60b) of Hsu *et al.* (1979) this is given by

$$b_{13} = \left(9\omega_0^{-4} - 6 + 2\omega_0^4\right)/16 - m^2\left(3\omega_0^{-8} + 5\right)/16 + n^2\left(3\omega_0^{-8} + 1\right)/16$$
$$+ \left[16\left(\gamma_1 \tanh(\gamma_1 kh) - \omega_0^2\right)\right]^{-1}\left[\left(-3\omega_0^{-6} + 8\omega_0^{-2} - 3\omega_0^2 + 2\omega_0^6\right) + m^2\left(-6\omega_0^{-6}\right.\right.$$
$$\left.\left. + 4\omega_0^{-2} - 10\omega_0^2\right) + n^2\left(6\omega_0^{-6} - 4\omega_0^{-2} - 2\omega_0^2\right) + 4n^2(m^2 - n^2)\omega_0^{-2}\right], \tag{5.1}$$

where $\omega_0 = \sqrt{\tanh(kh)}$, $m = \sin\theta$, $n = \cos\theta$ and $\gamma_1 = (m^2 + 9n^2)^{1/2}$. A comparison of the computed and theoretical beat amplitudes for variable θ is shown in figure 8, using the same series of simulations as in figure 7. Here the values of the spurious first harmonic amplitude a_B from the simulations have been estimated as half the total modulation from harmonic analyses similar to those shown in figure 5. These are then normalized appropriately (as indicated on the y-axis of figure 8) so that direct comparison with the theoretical b_{13} coefficient can be made. Again, the comparison results in a good match between the computed and theoretical results, with minor differences noticeable at large θ. Clearly, the importance of the responsible term grows considerably as θ approaches 90°, resulting in a similar increase in the amplitude of the spuriously generated first harmonic in simulations where the corresponding bound term has been neglected. This suggests that the first-harmonic modulation is likely to be much more easily observed at larger values of θ, consistent with the experimental observations of Hammack *et al.* (2005), which indeed used relatively large θ. It should be stressed, however, that the prediction of the beat amplitude using (5.1) will become increasingly inaccurate as $\theta \to 90°$, since the third-order perturbation expansion of Hsu *et al.* (1979), in fact, has a zero radius of convergence at this limit (see e.g. Roberts & Peregrine 1983). Note that for this reason, the simulated case with $\theta = 85°$ uses a slightly lower steepness ($ak = 0.10$, rather than $ak = 0.15$) which we find improves the match with the theoretical predictions.

This comparison further validates the theory developed in §4, in terms of both the beat length and amplitude, over a wide range of the incident angle θ.

6. Quantitative comparison with physical experiments

As further evidence that the present explanation is indeed responsible for the observed experimental features, we will now attempt a more quantitative comparison with the experiments of Hammack *et al.* (2005). Earlier comparisons of spuriously generated free harmonics from numerical models and experiments (in a single horizontal dimension) have been successfully made, e.g. in Mei (1983, figures 11.3 and 12.2), and Madsen & Sørensen (1993, figures 8 and 10), indicating that a reasonable match is indeed possible, despite the obvious differences between numerical and physical wave generation. Hammack *et al.* (2005) conducted a series of short-crested wave experiments (their C2–C8) similar to that presented in the previous section, where the angle θ was varied within the interval $77.7° < \theta < 86.9°$. Unfortunately, in most of these cases it is difficult to quantify accurately the beat length and amplitude, as the experiments were not designed specifically with this in mind. The phenomenon is particularly clear, however, from their figure 11(*a*), especially for cases C13 and C14 (with $ak = 0.35$ and 0.40, respectively), which closely resemble figure 4(*c*). We will therefore limit the current comparison to case C14 from the experiments, where the phenomenon is most apparent.

Figure 11(*a*) of Hammack *et al.* (2005) provides measured experimental time series from a centreline traverse at a speed of 0.1059 m s^{-1}. From their bottom sub-figure (case C14) a beat time of roughly 6.5 s may be estimated. This implies a beat length of $L_B \approx 0.1059 \text{ m s}^{-1} \times 6.5 \text{ s} = 0.688 \text{ m}$. Their experiment uses a wavenumber modulus $k = 64 \text{ m}^{-1}$, giving wavelength $L_x = 2\pi/(k \sin \theta) = 0.0995 \text{ m}$, which ultimately leads to the relative beat length $L_B \approx 6.9 L_x$. From figure 5(*c*) we measure $L_B = 7.1 L_x$, an excellent match. These measured/computed points are shown by $\times/\bigcirc$ on figure 7, where a reasonable, though not perfect, match with the theoretical curve can be seen. It is important to emphasize, however, that these particular experiments involve quite nonlinear waves, which as discussed earlier, lead to a reduction in the observed beat length. This reduction can be explained by inspecting the evolution equations for the harmonic amplitudes (see e.g. Madsen & Sørensen 1993), which reveal that (4.13) is only a first approximation, valid for small-amplitude wave–wave interactions.

Similarly, from the bottom sub-plot of figure 11(*a*) of Hammack *et al.* (2005), the amplitude of the spurious free first harmonic may be estimated (taking roughly half the difference between the high and low peaks of the modulating envelope) as $a_B \approx 0.0011 \text{ m}$, giving a dimensionless value of $a_B k \approx 0.070$. From the simulation of this case, figure 5(*c*), we measure a very close $a_B k = 0.067$. These measured and computed values respectively correspond to normalized dimensionless values of $2a_B/(a^3 k^2) \approx 2.2$ and 2.1, which are also shown on figure 8. Both values are significantly below the theoretical line (which again assumes weak nonlinearity), but are again quite similar to each other.

This comparison demonstrates a close match in both the beat length and amplitude between the numerical simulations and physical experiments. While further comparison with future experimental data is obviously desirable, this provides strong evidence that the previously described release of spurious free first harmonics, owing to the neglect of third-order contributions in the three-dimensional wave generation, is indeed the likely explanation of the observed experimental features.
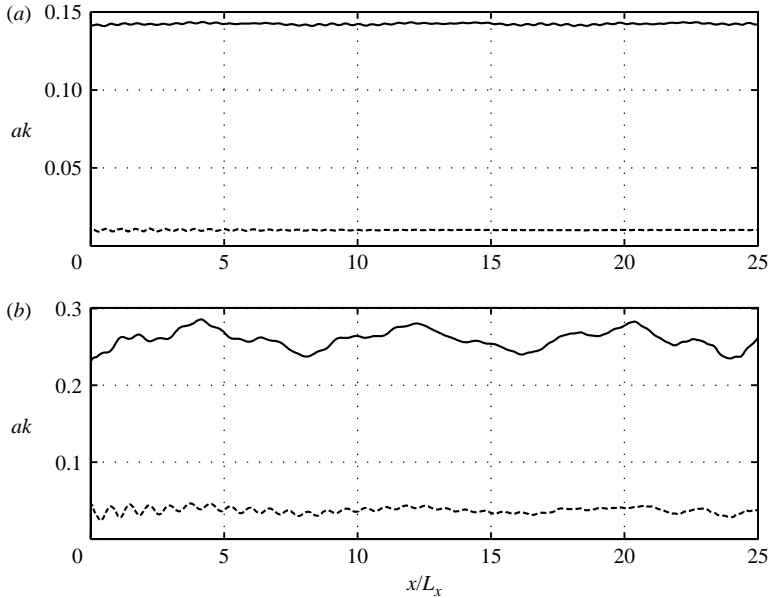
FIGURE 9. Computed first- (full line) and second- (dashed line) harmonic amplitudes from simulations using third-order incident conditions with (a) $ak = 0.15$ and (b) $ak = 0.30$.

7. Simulations using third-order incident conditions

As the physical explanation of the modulating phenomenon described in §4 stems from the absence of steady third-order contributions in the wave generation, it is of interest to consider simulations where these third-order contributions have been included in the generation. Therefore, figure 9 shows computed first and second harmonic amplitudes from a repeat of cases C9 and C12, where the general third-order bichromatic theory of Madsen & Fuhrman (2006) has now been used for the wave generation. This theory has been shown essentially to reduce to the steady third-order short-crested wave solution of Hsu *et al.* (1979) when the frequencies and amplitudes of the two input (first-order) waves are identical (Madsen & Fuhrman 2006). Additionally, this theory provides a means for determining the mean volume flux, which has been set to zero in the following simulations, to match conditions of a closed flume. The simulations again use $ak = 0.15$ and 0.30, where a is here the combined amplitude of the first-order components. Figure 9(a, b) can then be compared directly with figure 5(a, b).

In figure 9(a) the second harmonic amplitude is seen to be effectively constant across the entire computational domain, confirming the correctness of the generation to second order. The steadiness of the first harmonic amplitude is also significantly improved, further confirming the explanation from §4. Minor modulations are still evident, however, which generally become larger as the steepness is further increased, as seen in figure 9(b). These modulations, which share the same beat lengths as seen, e.g. in figure 5(b), can in fact be attributed to neglected higher-order effects. As evidence that this is indeed the case, we note that from figure 9(a) (with $ak = 0.15$) the dimensionless amplitude of the remaining first-harmonic beat is $a_B k = 0.0025$, whereas figure 9(b) (with $ak = 0.30$) yields $a_B k = 0.0484$. This implies a scaling of power $\log(0.0484/0.0025)/\log(0.3/0.15) = 4.26$, clear evidence that the remaining modulation is fourth order (and higher) in nature, which should be expected.
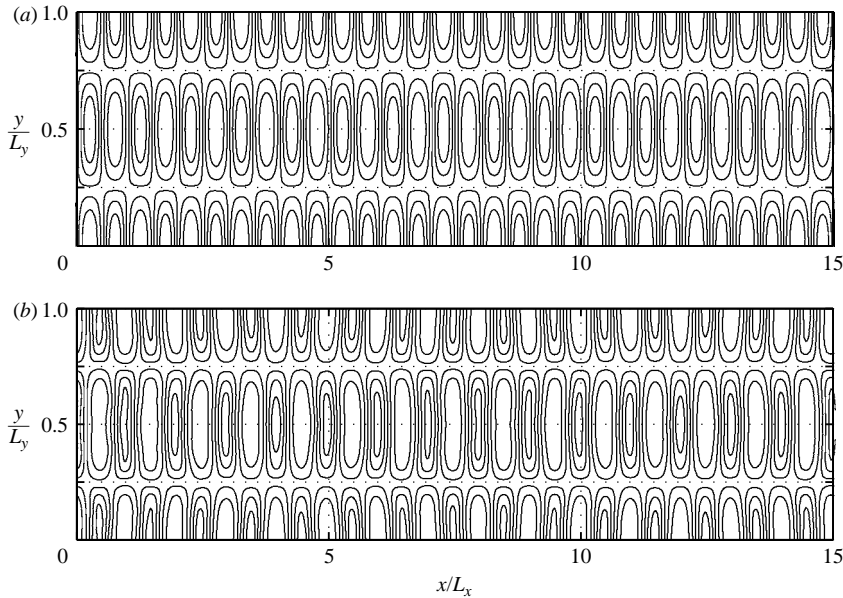
FIGURE 10. Computed contour plots from simulations using third-order incident conditions
with (a) $ak = 0.15$ and (b) $ak = 0.30$.

Computed contour plots from these two simulations are also shown in figure 10. These illustrate a significant improvement when compared to the previous simulations depicted in figure 3. The bending wave crests and peaks/dips along the centreline, which are so apparent, e.g. in figure 3(b), are now practically absent in figure 10(b). Hence, these simulations convincingly demonstrate that the addition of steady third-order components to the wave generation greatly reduces the previously described unsteady features. While higher-order steady solutions exist, e.g. from Roberts (1983) or Bryant (1985), for simplicity, the present demonstration will be limited to third-order incident conditions, as these are sufficient to confirm directly the explanation from §4.

8. Discussion

Hammack *et al.* (2005) provide qualitative explanations for many of their observed unsteady features. Specifically, they speculate that nearly all of their observed unsteady features (features 3–10 and 12 of their table 6), including the modulations in the x-direction and dips/flattening of the crestlines, can be explained via the (Benjamin–Feir type) instability of the observed patterns. We generally disagree with this explanation. Steady short-crested waves in deep water are indeed unstable to infinitesimal perturbations, as shown, e.g. by the analysis of Ioualalen & Kharif (1994) (see also Badulin *et al.* 1995; Kimmoun *et al.* 1999b). However, while analyses of the measured experimental time series, e.g. figure 11(b) of Hammack *et al.* (2005), do demonstrate minor unstable side-band growth, the detected side-band amplitudes are typically (at least) an order of magnitude smaller than that of the primary wave. This, therefore, cannot explain the severity of the observed modulations, which in some cases nearly reduce the amplitude of the centreline envelope to half, quite similar to figure 4(c). Additionally, it should be pointed out, that the modulation lengths

observed in the experiments are inconsistent with the group lengths that would be expected from the dominant (class Ia) short-crested wave instabilities found, e.g. by Ioualalen & Kharif (1994) and Kimmoun *et al.* (1999*b*).

That the modulations, in both the simulations and experiments, begin immediately after the wave generation is further evidence of their cause being the release of spurious harmonics, as Benjamin–Feir-type instabilities typically require long distances to develop. Note also that, as short-crested wave instabilities are generally weaker than their plane wave counterparts (Ioualalen & Kharif 1994), they should correspondingly require an even longer distance to develop from experimental background noise. Moreover, we have performed additional long-time fully nonlinear numerical simulations of both class Ia and Ib short-crested wave instabilities (see Fuhrman, Madsen & Bingham 2006). These typically lead, for example, to a quasi-recurrence cycle (of typically $O(100)$ wavelengths) or a frequency downshift, with results depending somewhat on the incident wave nonlinearity, i.e. the unstable evolution is qualitatively different from those observed here or in the experiments of Hammack *et al.* (2005).

Hammack *et al.* (2005) also claim that steady third-order solutions for short-crested waves (with large θ) can alternatively explain the observed dips along the centreline, when the steepness is sufficiently large. There are two principal shortcomings with this explanation, however. First, as already acknowledged by Hammack *et al.* (2005), the observed dips were, in fact, not steady. Secondly, the presence of centreline dips in a steady third-order solution indicates that the theory is no longer valid, and that higher-order effects (or a different expansion, as in Roberts & Peregrine 1983) should be taken into account, which will in turn straighten out the crests. This is illustrated, for example, in figure 7(*d*) of Roberts (1983), figures 4 and 5 of Roberts & Peregrine (1983), and figure 7 of Bryant (1985), which show highly nonlinear steady deep-water short-crested wave patterns with straight crests and large θ.

Additionally, the bending of the crestlines is likewise explained by Hammack *et al.* (2005) within the context of steady third-order solutions. However, these solutions (at sufficient steepness) exhibit simultaneous frontward and backward bending of a given crest (each crest being front–back symmetric, see e.g. their figure 20*a*), whereas the experimental pictures demonstrate crests bending either frontwards or backwards at a given instant, similar to those shown in figures 2 and 3. Higher-order steady contributions will likewise remove such bending, as is apparent from the previously mentioned figures from the literature.

Thus, Hammack *et al.* (2005) correctly predict that many of the features are indeed third-order in nature, but do not account for the release of spurious free first harmonics as a consequence of using first-order wavemaker conditions. The close match (both qualitatively and quantitatively) between the simulations presented here and the physical observations of Hammack *et al.* (2005) provides strong evidence that this is indeed the proper explanation of the most pronounced unsteady features observed in the experiments (i.e. long modulations, dipping at the wave crests, and curving crestlines). Furthermore, this simple explanation removes the previously noted discrepancies, while also demonstrating how these various features are in fact closely related to one another.

As the use of first-order wavemaker conditions is commonplace in wavetank experiments involving short-crested waves, the recognition of this phenomenon is fundamentally important to both experimentalists and numerical modellers alike. That a low-order short-crested (three-dimensional) wave generation can directly affect the spatial evolution of the primary frequency, inducing a long modulation, is particularly troublesome from an experimental viewpoint, as the measured wave

amplitude can in turn vary dramatically depending on the location. As can be seen from figure 4(*b, c*) and figure 5(*b, c*), the effects due to this third-order contribution can be quite pronounced (even dominant), particularly when the wave steepness becomes moderately large. Indeed, based on our numerical results, which are likewise supported by the physical experiments, it is seemingly impossible to generate reasonably steady progressive short-crested waves (of even moderate steepness) at large incident angles ($\theta > 70.53°$) without taking into account third-order effects in the wave generation. This work therefore makes apparent the need for a third-order (three-dimensional) wavemaker theory, before the phenomenon of truly progressive finite-amplitude short-crested waves (at large θ) can be more reliably studied in experimental wavetanks. Currently, wavemaker theory has only been developed to second-order (see e.g. Schäffer 1996; Schäffer & Steenberg 2003), which is already rather complicated. As this phenomenon has been shown to occur in the generation of monochromatic short-crested waves (i.e. the simplest three-dimensional waves) there are also likely to be related consequences in more general three-dimensional wave generation, though we will not specifically pursue them here.

It should finally be mentioned that Hammack *et al.* (2005) describe an additional series of experiments using a Jacobi elliptic sine function in the transverse direction. It seems likely that spurious free first harmonics were likewise generated in these experiments, as modulations in the propagating direction, curving of the crestlines, and centreline dips are also reported in these experiments. This is consistent with the present explanation. In principle, any generation of finite-amplitude short-crested waves (with $\theta > 70.53°$) which does not strictly satisfy the wavemaker problem to third order will suffer, in some degree, from this phenomenon. Given the previous results, it is also likely that even higher-order effects might become important, depending on the desired wave steepness and incident angle θ. Their consideration is beyond the scope of the present work, however.

9. Conclusions

A numerical model based on a high-order Boussinesq-type formulation has been used to study dynamics related to the generation of monochromatic short-crested wave patterns in deep water. To approximate conditions from a series of recent physical experiments from Hammack *et al.* (2005), linear (sinusoidal) doubly periodic wavemaker conditions have been imposed as incident conditions in the nonlinear numerical model under a variety of wave steepnesses and incident angles. The simulated wavefields share many common features with the experiments, including bending (both frontwards and backwards) of the wave crests, dips along the centreline, and a pronounced long modulation along the direction of propagation. The modulation has been isolated as the driving mechanism of the other features.

The consequences of such a first-order short-crested wave generation (for finite-amplitude waves) have, for the first time, been systematically assessed. From the combined simulations and analysis, the modulating phenomenon is demonstrated to arise, not from a Benjamin–Feir-type instability as previously speculated, but from a non-intuitive, yet inevitable, release of free first harmonics due to neglected third-order components in the wave generation. The phenomenon is due entirely to the three-dimensionality of the problem, and will disappear (i.e. become infinitely long) at the plane wave limit. It is also limited to the generation of short-crested waves at relatively large incident angles (theoretically for $\theta > 70.53°$), consistent with the experimental conditions where it was apparently observed. A comparison of the

numerical/theoretical beat length and amplitude with the measurements confirms this explanation. Inclusion of steady third-order contributions in the incident wavefield has additionally been shown to reduce greatly the first-harmonic modulation (and other unsteady features), providing yet further confirmation.

This work reveals previously unrecognized difficulties in the physical generation of even the simplest three-dimensional waves, which must be overcome before steady, moderately steep short-crested waves can be more reliably generated in physical wavetanks. This work also serves as a good demonstration of the ability of direct numerical simulation (combined with analysis) to provide significant insight into the interpretation of physical (experimental) observations.

REFERENCES

BADULIN, S. I., SHRIRA, V. I., KHARIF, C. & IOUALALEN, M. 1995 On two approaches to the problem of instability of short-crested water waves. *J. Fluid Mech.* **303**, 297–326.

BENJAMIN, T. B. & FEIR, J. E. 1967 The disintegration of wave trains on deep water. Part 1. Theory. *J. Fluid Mech.* **27**, 417–430.

BOCZAR-KARAKIEWICZ, B. 1972 Transformation of wave profile in shallow water – a Fourier analysis. *Arch. Hydrotechnik* **19**, 197–210.

BRYANT, P. J. 1973 Periodic waves in shallow water. *J. Fluid Mech.* **59**, 625–644.

BRYANT, P. J. 1985 Doubly periodic progressive permanent waves in deep water. *J. Fluid Mech.* **161**, 27–42.

BUHR-HANSEN, J. & SVENDSEN, I. A. 1974 Laboratory generation of waves of constant form. In *Proc. 14th Coastal Engng Conf.* pp. 320–338. Copenhagen.

CHAPALAIN, G., COINTE, R. & TEMPERVILLE, A. 1992 Observed and modelled resonantly interacting progressive water waves. *Coast. Engng* **16**, 267–301.

CHEN, Y. & LIU, P. L.-F. 1995 Modified Boussinesq equations and associated parabolic models for water wave propagation. *J. Fluid Mech.* **288**, 351–381.

CRAIG, W. & NICHOLLS, D. P. 2002 Traveling gravity water waves in two and three dimensions. *Eur. J. Mech.* B/*Fluids* **21**, 615–641.

FENTON, J. D. 1985 Wave forces on vertical walls. *J. Waterways Port C-ASCE* **111**, 693–718.

FUHRMAN, D. R. & BINGHAM, H. B. 2004 Numerical solutions of fully non-linear and highly dispersive Boussinesq equations in two horizontal dimensions. *Intl J. Numer. Meth. Fluids* **44**, 231–255.

FUHRMAN, D. R., BINGHAM, H. B., MADSEN, P. A. & THOMSEN, P. G. 2004*a* Linear and non-linear stability analysis for finite difference discretizations of high-order Boussinesq equations. *Intl J. Numer. Meth. Fluids* **45**, 751–773.

FUHRMAN, D. R., MADSEN, P. A. & BINGHAM, H. B. 2004*b* A numerical study of crescent waves. *J. Fluid Mech.* **513**, 309–341.

FUHRMAN, D. R., BINGHAM, H. B. & MADSEN, P. A. 2005 Nonlinear wave–structure interactions with a high-order Boussinesq model. *Coast. Engng* **52**, 655–672.

FUHRMAN, D. R., MADSEN, P. A. & BINGHAM, H. B. 2006 Numerical simulation of lowest-order short-crested wave instabilities. *J. Fluid Mech.* (in press).

HAMMACK, J. L. & HENDERSON, D. M. 2003 Experiments on deep-water waves with two-dimensional surface patterns. *J. Offshore Mech. Arctic Engng* **125**, 48–53.

HAMMACK, J., SCHEFFNER, N. & SEGUR, H. 1989 Two-dimensional periodic waves in shallow water. *J. Fluid Mech.* **209**, 567–589.

HAMMACK, J., MCCALLISTER, D., SCHEFFNER, N. & SEGUR, H. 1995 Two-dimensional periodic waves in shallow water. Part 2. Asymmetric waves. *J. Fluid Mech.* **285**, 95–122.

HAMMACK, J. L., HENDERSON, D. M. & SEGUR, H. 2005 Progressive waves with persistent two-dimensional surface patterns in deep water. *J. Fluid Mech.* **532**, 1–52.

HSU, J. R., TSUCHIYA, Y. & SILVESTER, R. 1979 Third-order approximation to short-crested waves. *J. Fluid Mech.* **90**, 179–196.

IOUALALEN, M. 1993 Fourth order aproximation of short-crested waves. *C. R. Acad. Sci. Paris, Série II* **316**, 1193–1200.

IOUALALEN, M. & KHARIF, C. 1994 On the subharmonic instability of steady three-dimensional deep water waves. *J. Fluid Mech.* **262**, 265–291.

KIMMOUN, O., BRANGER, H. & KHARIF, C. 1999a On short-crested waves: experimental and analytical investigations. *Eur. J. Mech.* B/*Fluids* **18**, 889–930.

KIMMOUN, O., IOUALALEN, M. & KHARIF, C. 1999b Instabilities of steep short-crested surface waves in deep water. *Phys. Fluids* **11**, 1679–1681.

MADSEN, P. A. & FUHRMAN, D. R. 2006 Third-order theory for bichromatic bi-directional water waves. *J. Fluid Mech.* **557**, 369–397.

MADSEN, P. A. & SØRENSEN, O. R. 1993 Bound waves and triad interactions in shallow water. *Ocean Engng* **20**, 359–388.

MADSEN, P. A., BINGHAM, H. B. & LIU, H. 2002 A new Boussinesq method for fully nonlinear waves from shallow to deep water. *J. Fluid Mech.* **462**, 1–30.

MADSEN, P. A., BINGHAM, H. B. & SCHÄFFER, H. A. 2003 Boussinesq-type formulations for fully nonlinear and extremely dispersive water waves: derivation and analysis. *Proc. R. Soc. Lond.* A **459**, 1075–1104.

MADSEN, P. A., FUHRMAN, D. R. & WANG, B. 2006 A Boussinesq-type method for fully nonlinear waves interacting with a rapidly varying bathymetry. *Coast. Engng* **53**, 487–504.

MEI, C. C. 1983 *The Applied Dyamics of Ocean Surface Waves*. John Wiley.

MEI, C. C. & ÜNLÜATA, U. 1972 Harmonic generation in shallow water waves. In *Waves on Beaches and Resulting Sediment Transport* (ed. R. E. Meyer), pp. 181–202. Academic.

NICHOLLS, D. P. 1998 Traveling water waves: spectral continuation methods with parallel implementation. *J. Comput. Phys.* **142**, 224–240.

NICHOLLS, D. P. 2001 On hexagonal gravity water waves. *Math. Comput. Simulation* **55**, 567–575.

ROBERTS, A. J. 1983 Highly nonlinear short-crested water waves. *J. Fluid Mech.* **135**, 301–321.

ROBERTS, A. J. & PEREGRINE, D. H. 1983 Notes on long-crested water waves. *J. Fluid Mech.* **135**, 323–335.

SAVITZKY, A. & GOLAY, M. J. E. 1964 Smoothing and differentiation of data by simplified least squares procedures. *Anal. Chem.* **36**, 1627–1639.

SCHÄFFER, H. A. 1996 Second-order wavemaker theory for irregular waves. *Ocean Engng* **23**, 47–88.

SCHÄFFER, H. A. & STEENBERG, C. M. 2003 Second-order wavemaker theory for multidirectional waves. *Ocean Engng* **30**, 1203–1231.